

BEYOND GEO: STRATEGIES FOR MONITORING CISLUNAR ENVIRONMENT

Jonko Paetzold^(1*,2), Pia Lenhardt⁽²⁾, Marc Torras Ribell⁽¹⁾, Simon Burgis⁽²⁾, Reinhold Bertrand⁽³⁾, Eduardo Arias Ruíz-Escribano⁽⁴⁾, Francisco Javier Simarro Mecinas⁽⁴⁾, and Alejandro Pastor⁽¹⁾

¹GMV, Europaplatz 2, 64293 Darmstadt, Germany, *Email: jpaetzold@GMV.com

²Institute of Flight Systems and Automatic Control, Technical University of Darmstadt, Otto-Berndt-Straße 2, 64287 Darmstadt, Germany

³Joint Professorship Space Systems Between Institute of Flight Systems and Automatic Control and European Space Agency ESA/ ESOC, TU Darmstadt, Otto-Berndt-Straße 2, 64287 Darmstadt, Germany

⁴GMV, Isaac Newton 11, 28670 Tres Cantos, Madrid, Spain

ABSTRACT

The cislunar region, governed by both Earth's and the Moon's gravitational forces, presents unique challenges for space surveillance and tracking. Traditional near-Earth monitoring systems face difficulties with the complex orbital dynamics and vast spatial scale of this environment. With over a hundred missions planned in the coming decade, improved coordination and sensor tasking strategies are crucial for operational safety. This paper explores the limitations of existing systems and methodologies, and evaluates sensor networks for cislunar tracking, leveraging ESA's (European Space Agency) GODOT library for orbital modelling and analysis.

1. INTRODUCTION

Cislunar space, extending from Earth's geostationary orbit (GEO) to beyond the Moon [2, 6, 8], is poised to become an area of significant mission activity. Unlike near-Earth space, where the dynamics are approximated using two-body orbital mechanics, cislunar dynamics require a three-body problem approach due to the gravitational influence of both the Earth and the Moon. The resulting orbits, including libration point trajectories, Lyapunov orbits, and Halo orbits, exhibit non-repeating, chaotic characteristics that challenge conventional space surveillance methods.

Programmes such as ARTEMIS [11] and the Chang'E programme [17] show that the interest in lunar exploration is growing. This is not just leading to an increase in governmental missions to the cislunar region, but also commercial missions such as the upcoming Intuitive Machines 3 lunar lander, scheduled for launch in October 2025 [13] as part of NASA's (National Aeronautics and Space Administration) Commercial Lunar Payload Services programme [12]. This increase in traffic in the region in the coming years

will require the establishment of reliable tracking and coordination mechanisms.

Existing space monitoring systems, like the US American Space Surveillance Network (SSN) [9] or the European Union Space Surveillance and Tracking (EU SST) program [14], optimized for near-Earth operations, face fundamental limitations when applied to cislunar tracking. The increased distance of existing Earth-based and Earth orbiting sensors from the region of interest results in a significant degradation of signal strength for the observing sensors. In addition, the relative motion of the Earth, Moon and Sun further limits the time during which the region is visible to the observer. For Earth orbiting sensors the occultation by the Earth restricts visibility once per orbital period while ground-based observers are even further limited by the day and night cycle on Earth's surface. [8]

By positioning sensors close to the cislunar region, either in cislunar orbits or on the lunar surface itself, the limitation of low signal strength can be mitigated. While this approach addresses the problem of signal strength, it introduces other complications, the most obvious being the added complexity of setting up and operating such a sensor. To overcome the problem of limited visibility intervals due to occultation and blinding of the sensor by celestial bodies, a network of sensors can be used, achieving high observability times of the region. [8]

While the motion of objects in the three-body dynamics dominated space of the cislunar region is inherently unstable, simplified models like the Circular Restricted Three Body Problem (CR3BP) can be utilised to find repeating orbits, useful for the preliminary design of missions. The repeating orbits resulting from the CR3BP can be classified into orbit families, whose members are defined by their stability index, the Jacobi constant, representing the orbital energy, and their period. [5]

Certain families of repeating orbits are better suited to observe the cislunar region than others. In particular, Distant Retrograde Orbits (DRO) and Lyapunov orbits

are well suited to cislunar observations due to their inherent stability and orbital paths that cover large parts of the region. [6]

By optimising for different criteria, like orbit stability and observational capabilities, a study by Badura et al. [1] found various possible networks of orbiting cislunar sensors. The networks consist of different numbers of sensors on different repeating orbits of the DRO, Lyapunov and Halo orbit families.

While there has been previous work on the observation of the cislunar region, less work has been done to evaluate the tracking capabilities of different cislunar sensor networks in the context of Space Situational Awareness (SSA) and Space Surveillance and Tracking (SST). Therefore, this paper presents the first results of a model for simulating cislunar sensor networks using CR3BP dynamics, developed as a tool to investigate the tracking and surveillance capabilities of space and ground-based sensor networks. Using ESA's (European Space Agency) astrodynamics library GODOT [4], different sensor placements including Earth-based, space-based, and lunar surface-based observers are analysed with the aim of assessing their effectiveness in mitigating tracking challenges and enhancing situational awareness in the cislunar domain.

A number of different sensor technologies can be used for observing the cislunar region and space objects in general. Most of the commonly used sensors can be categorised into electro optical and radio frequency based sensors. These categories can be further subdivided into active and passive sensors. Passive sensors have the clear advantage of significantly lower power requirements, being especially relevant for remote sensors in cislunar orbit or the lunar surface [8]. On the other hand, passive sensors have the disadvantage of relying on external sources reflecting off of target objects or the target object itself emitting a signal for enabling observation. While some target objects emit detectable radio signals, every object will reflect some light emitted by the Sun, making it detectable by passive optical sensors like telescopes. While all mentioned possible sensor technologies could be used for observing cislunar space objects, this paper only investigates passive electro optical sensors due to their widespread use and flexibility in SSA and SST operations.

This paper starts by outlining assumptions and fundamentals used in the model in Section 2 before giving an overview of the model framework in Section 3. Next, some analysis runs are set up and explained, and their results discussed in Section 4. Finally, in Section 5, a conclusion is drawn from the preliminary results achieved by the model and the next steps are outlined.

2. ASSUMPTIONS AND THEORETICAL FOUNDATIONS

To model the cislunar region and its inhabitants a physical simulation model is created for analysing the positions and interactions between different objects and bodies in this region. There is a multitude of influences on the behaviour of objects in space, like solar radiation pressure, non-spherical gravitational effects from the Earth and the Moon, and the gravitational influence of other celestial bodies in the solar system, predominantly by the Sun and Jupiter. Due to the complex nature of considering all these effects, some simplifications are made concerning the forces acting on these objects.

To simplify the orbital motion of space objects, the CR3BP is utilized ignoring the influence of all other celestial bodies except for the Earth and the Moon. Perturbations caused by the non-spherical gravitation of Earth and Moon are also not considered. Additionally, forces acting on the object due to solar radiation pressure or the atmosphere are also ignored. This approach is comparable to using Keplerian two body dynamics for modelling orbits around Earth, ignoring all other perturbations like drag, solar radiation pressure, non-spherical dynamics and three-body perturbations.

2.1. The Circular Restricted Three Body Problem and the synodic reference frame

The CR3BP represents a simplified model for the orbital motion of a system of three bodies with mass. While a three-body system normally displays chaotic behaviour the CR3BP uses some simplifications to create a simpler model for the motion of an object being perturbed by two massive bodies. For this, there are two main assumptions [16]:

1. The mass of the object is negligible in comparison to the two massive bodies and can be ignored.
2. The two massive bodies are moving on circular orbits around their common barycenter.

As the two bodies are moving on circular paths with the same orbital period, the distance between the bodies, as well as the distance of each body to the barycenter, stays constant at all time. This allows for the definition of a synodic reference frame which is rotating together with the Earth-Moon-system. The origin of this frame is defined to be in the barycenter with its X-axis pointing towards the Moon and its Z-axis pointing out of the Earth-Moon-system's rotational plane as seen in Figure 1. It is also common to scale the length and time units of the reference frame to be dimensionless. The distance between the two massive bodies is used as the reference length unit, and the period of the orbits of the massive bodies is used as the reference time.

Using these reference values, all related values are made dimensionless. All further measurements in this work will be given in this non-dimensional reference frame unless stated otherwise.

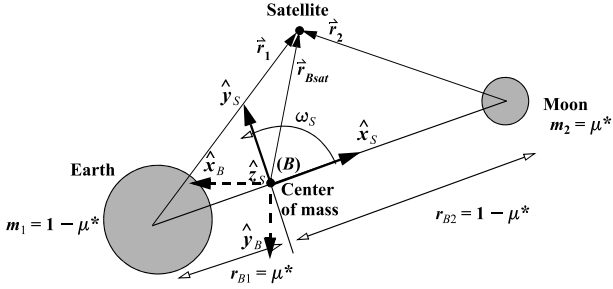


Figure 1: Definition of the synodic reference frame showing the placement and orientation of the reference axes in the Earth-Moon barycenter with the X-axis pointing towards the Moon and Z-axis pointing out of the rotational plane. Figure extracted from [16].

2.2. Optical observability of objects

The optical observability of an object is dependent on multiple factors such as the relative position of the observer and the object, the relative positioning of different celestial bodies to their position, as well as the physical attributes of the object and the capabilities of the observer. To evaluate if an object is visible to an observer at a given epoch, a number of observability constraints are used. These include the apparent magnitude of the object in conjunction with the minimal detectable magnitude of the observer, occultations by the Earth and the Moon, as well as exclusion zones due to sensor blowout by large bright objects like the Sun. This section aims to further detail the effects at work for these observability limits.

2.2.1. Apparent magnitude calculation

The apparent magnitude is a measure for the amount of light emitted or reflected by an object which can be perceived by an observer. For an illuminated object like a satellite this depends on the distance of the object to the observer, the reflectivity and shape of the object, as well as the phase angle between the observer, the object and the illumination source.

For actual space objects, the attitude of the object is also of importance as it influences the direction in which light is reflected as well as the projected area from the position of the observer. As modelling of the geometry and attitude of every observed object adds significant computational effort, it is omitted from this work. All objects are therefore assumed to be spherical. Further, Lambertian reflectance is assumed for all objects [15].

Using these simplifications, an expression for calculating the apparent magnitude m_{app} of an object to an observer is derived:

$$m_{app} = m_S - 2.5 \log_{10} \left(\frac{2}{3\pi^2} \cdot A \cdot \rho \cdot \Theta \right) + 5 \log_{10}(d) \quad (1)$$

m_S represents the apparent magnitude of the illuminating object to the observed object and A , ρ and d represent the projected area, the albedo and the distance between the observer of the target object respectively. In this work only the Sun's illumination is considered. Due to the small relative changes in distance to the Sun for all considered objects this distance is assumed to be constant at 1 au resulting in a constant apparent magnitude of the Sun of $m_S = -26.74$. [2, 7]

The phase function Θ is used to model the influence of the phase angle between the observer, the observed object and the Sun:

$$\Theta(\varphi) = (\pi - \varphi) \cdot \cos(\varphi) + \sin(\varphi) \quad (2)$$

with the phase angle φ representing the angle between the observer, the target and the Sun, as the illumination source. [2, 7]

2.2.2. Occultations and white outs

Occultations happen when a celestial body is blocking the line of sight of an observer to a target. A white out on the other hand describes the overexposure of an optical sensor due to a bright object, rendering it useless in observing a target. While the mechanism hindering the observations in these two cases is very different, the two effects can be modelled in a very similar way. In both cases the connection vector from the observer to the target coincides with the connection vector from the observer to the celestial body.

As the celestial body is not just a single point but occupies a certain area in the field of view of the observer, its angular size has to be considered. In case of the white out it is also not possible to observe objects in the vicinity of the bright body, leading to a further expansion of the exclusion zone around the body. In case of an occultation the target also has to be behind the occulting body. By calculating the distance both from the observer to the target and from the observer to the celestial body and comparing these two distances, the target position is derived to be in front or behind the occulting body.

This work considers three celestial bodies for possible occultations and white outs: The Earth, the Moon and the Sun. In case of the Sun, occultations are not

possible in the considered region as it is too far away. White outs on the other hand are significant due to the Sun's brightness. In case of the Earth and the Moon, occultations are possible and have to be considered. Due to their illumination by the Sun and their size, the Earth and the Moon also have to be considered for creating white outs in optical sensors as they are bright enough to overshadow any signal coming from a target. When considering white outs for these two bodies, any observability limitation coming from occultations is already contained in the limitation set by the white out exclusion zones, and therefore does not have to be computed additionally. All visibility restrictions due to the Earth, the Moon and the Sun can therefore be represented by exclusion zones around the respective body. These exclusion zones are set to 30°, 35° and 50° for the Earth, the Moon and the Sun respectively [2].

3. METHODOLOGY

For the analysis of different sensors and sensor networks, a simulation framework is implemented utilizing ESA's flight dynamics library GODOT. Its basic structure is illustrated in Figure 2 and the related workflow is described in Section 3.2.

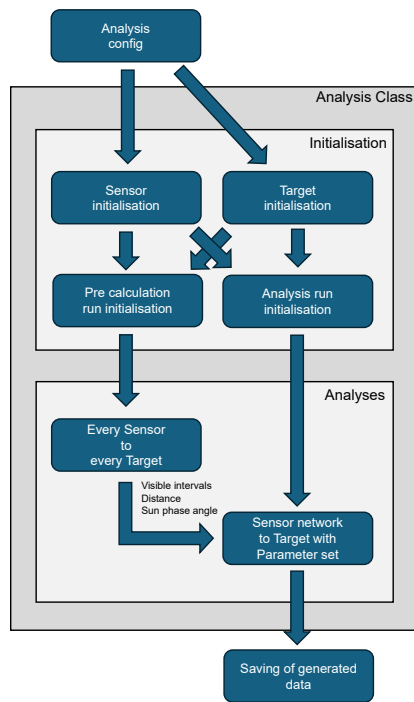


Figure 2: Inner workflow of the analysis class from input of the analysis configuration to the output of the generated data.

Each analysis run is conducted in two steps. First, in the initialisation step, an environment according to the configuration input is created. This includes the set up of the reference frame, the target and sensor objects, as

well as the import and propagation of initial states of the objects on repeating cislunar orbits. This is followed by the analysis step that conducts the sensor tasking analysis and saves the analysis output for further use and visualisation.

In the following, the different configuration options and creation of input files are described in more detail as well as the definition and the simulation workflow of an analysis run.

3.1. Analysis setup configuration

To set up an analysis run, all the necessary configurations to execute that run have to be supplied. The configuration file contains not just the information about the settings for the run itself but also the information necessary for initialising the environment as well as the target and sensor objects used for the run. This includes:

- configurations for setting up the model system as well as reference systems like a GODOT universe,
- paths to resources like the initial states for repeating orbits,
- settings for the different sensor and target objects as well as
- the definition of the actual analyses that are to be run.

This section will go into further detail on the initialisation of the different objects as well as the analysis itself.

3.1.1. Initial states for repeating orbits

Before any orbiting objects can be initialised, their orbits have to be defined. As the cislunar region is heavily influenced by three-body dynamics, orbits can not be approximated using Keplerian mechanics. Therefore, the CR3BP model, previously mentioned in Section 2.1, is used to describe the dynamics of the system.

By using the simplifications of the CR3BP, repeating orbits can be found in the dynamical model. While these orbits are repeating using the CR3BP, they are only stable as long as perturbations like drag, solar radiation pressure and the influence of other massive bodies is neglected. This leads to station keeping efforts in the actual deployment of objects in orbits governed by three-body dynamics. Nevertheless, these families of repeating orbits give a good first reference for designing missions in this region. [1]

To include objects using these repeating orbits, they first have to be defined. For this, JPL (Jet Propulsion Laboratory) created a web tool for finding and

downloading initial states for repeating orbits in the CR3BP [10]. After the desired initial states are selected, they are propagated over one orbital period and used as a reference for the satellite state.

3.1.2. Sensor definition

To analyse a sensor or sensor network, the sensors themselves have to be defined. Two main types of sensors are considered: Orbiting sensors defined as satellites and ground-based sensors defined as ground stations, either on the surface of the Earth or the Moon.

To define an orbiting sensor, the desired orbit as well as a reference epoch is given and a reference name is assigned to relate to it in the analysis setup. The sensor's orbit is then defined using an initial state at the reference epoch. The desired initial state is loaded and the orbit is propagated from the reference period onward to find the state of the sensor at a specific epoch. Further capabilities of the sensor are not defined at this step, but later in the the analysis set up, as this gives more flexibility in defining the parameters for an analysis run.

For the definition of ground stations a distinction is made for Earth-based and Moon-based ground stations. As the Moon is tidally locked to the Earth and the synodic reference frame used for the analysis is also locked to the Moon's orbit, the Moon only shows very little movement in the defined reference frame. The position of a lunar ground-based sensor can therefore be defined using two angles for latitude and longitude on the Moon's surface. [3]

On the other hand, ground-based sensors on the surface of the Earth have to be defined in a different way due to Earth's rotation in the used reference frame. For this, the station functionality of GODOT is utilised. By defining a name and the location of the ground station in an Earth fixed reference frame, it can then be loaded when a GODOT universe is created. Using the defined name of the station, its location and zenith direction is retrieved from the GODOT universe and transformed into the synodic reference frame.

Similar to the orbital sensors, all further capabilities of the ground-based sensors are defined in the analysis configuration in a later step in order to enable better control of parameters in an analysis run. The parameters concerned with the sensor capabilities include the minimal apparent magnitude that is observable by the sensor, as well as the positional uncertainty and the uncertainty of an optical measurement. Further, for ground-based sensors a horizon is defined up to which they are capable of observing a target.

3.1.3. Target definition

In addition to the sensors, the targets to observe have to be configured as well. There are two main types of targets:

The first type is an orbiting target which is configured and defined in the same way as an orbiting sensor, as described in Section 3.1.2. For this, an orbit is selected before it is propagated starting from the respective initial state downloaded from the JPL website, as described in Section 3.1.1.

The second target type consists of a grid of stationary points in an area of the cislunar space. This allows for a more general overview of a network's capabilities over a region in cislunar space. To define the equidistant points of the grid a centre point, the range in all three directions and a step size is chosen and the grid is generated. After the grid is created, each point is used as a stationary target to observe.

Similar to the sensor definitions, further target properties are defined later on rather than at the initialisation step to keep the possibility of setting parameters differently for different analyses. These parameters include the object radius and its reflectivity.

3.1.4. Analysis definition

After all the required sensors and targets are defined, the analysis run itself is configured. For this, a set of sensors representing the sensor network to be analysed and a timespan over which it is to be analysed is defined. Some further parameters are then defined as listed below:

- **Targets:** This represents the target or targets to be observed by the sensors. Any previously defined target or target grid can be used here.
- **Target radius:** The radius of the Lambert sphere used as a model for the target's size.
- **Magnitude threshold:** The minimal detectable apparent magnitude for the sensors.
- **Sensor measurements noise:** A measure for the noise of the optical sensors represented by the standard deviation in the measured angles to the target.
- **Position uncertainty:** A characterisation for the positional uncertainty of the sensors represented by the standard deviation in the known position of the object. This is always assumed to be zero for ground-based sensors.

Each of the listed parameters can be set to a single value or a set of values. In case sets of values are defined for one or more parameters, all possible permutations

of all sets are used to create separate analysis run instances. This provides an easy way of running either a single analysis or large parameter studies for a defined sensor network. To analyse different sensor networks, a new entry is created in the analysis definition for each sensor network. After all desired analyses and their requirements are defined, an analysis can be run using the defined configurations.

3.2. Analysis execution

The previous sections described the set up of the configuration file for an analysis run. In the initialisation step of the analysis, the sensors and targets defined in the configuration file, as well as the analysis run and the pre-calculation run are initialised, as can be seen in Figure 2. As each analysis of a sensor network to a target uses the same underlying base data for visibility, independent of the different additional object parameters given, a pre-calculation step is done after the initialisation step for better runtime. This can be seen in the first step in the analyses step in Figure 2. In this step, every possible sensor-target combination is extracted from all analysis configurations. Each pair of sensors and targets is then analysed over the longest epoch range possible using the given analyses. The intervals in this epoch range in which the target is not occulted or blinded by the Earth, the Moon or the Sun is found using GODOT's root finding algorithms. The algorithm finds event interval sets in which a certain restriction applies, like in this case an occultation or white out. These interval sets are then combined using boolean logic to arrive at an interval set containing all epochs of visibility for the specified sensor-target pair. Following this, the distance from sensor to target as well as the phase angle of the the sensor, the target and the Sun are calculated for each epoch in the visible intervals of the full epoch range.

After the pre-calculation step, the produced data is used to find the final visibility of a target to a sensor considering its magnitude defined by the additional object parameters. Using the calculated distance and phase angle together with the current target radius, the apparent magnitude is calculated. With the minimal detectable magnitude set in the configuration file this gives a further criterion for the possible visibility of the target by the sensor. The reason for not already calculating this visibility cut off in the pre-calculation step is the gained flexibility in analysing multiple parameter sets. After the final visibility epochs for the target are calculated, the positions of the sensor to the target are used in conjunction with the sensor noise and positional uncertainty of the sensor to arrive at a combined measurement uncertainty of the target.

All calculations to this point have been performed for pairs of one sensor and one target. By combining multiple of these pairs the capabilities of the full sensor network can be calculated. For each epoch in the range all available sensors in the network are loaded and the best

performing result is selected. If no sensor is available at an epoch, this epoch is marked as not observable by the network. This approach results in a quality metric for all single satellites in the network as well as for the combined sensor network, which is saved for further investigation and evaluation.

4. ANALYSIS RESULTS AND DISCUSSION

To evaluate the model and its results, analyses are set up and run. For this, testcases are defined according to the workflow described in Section 3.1. Three main cases are explored in this work which include Earth-centred, Moon-based and orbital cislunar sensors. To evaluate these different sensors and sensor networks, they are analysed towards two different targets. The first target consists of a grid of target points centred around the Moon to gain a general overview of the sensors' capabilities. Secondly, a Moon-centred object is used as a target, as an example for analysing the coverage of a specific object using the model. This section firstly discusses the two targets chosen for analysis in Section 4.1 before discussing the three main testcases and their results in Section 4.2, 4.3 and 4.4. The used sensors and targets are detailed further in the following.

While different assumptions are made for the different cases, some overarching settings are used for all analysis runs. For the observability limit due to the apparent magnitude of a target to an observer a minimal detectable magnitude of 18 is used for all observers. The radius of all observed objects is further assumed to be 1 m with the targets having an albedo of 0.2. [1]

Further, all analysis runs are performed over the duration of one year with a time step of one hour. This is done to get a reasonable average of the different Sun positions and illumination conditions in the observed region. [1]

4.1. Targets used for the analyses

The first target, represented by a grid of target points, aims to give an overview of the general performance and capabilities of the tested sensor networks. For this, a Moon-centred grid is chosen to serve as a representative area in the cislunar region [1]. The used grid spans out from the Moon with a maximum radius of 150 000 km, with an equal grid point spacing of 30 000 km. This discretises the region into a total of 573 target points.

To show the analysis capabilities of the model using a specific object, an exemplary repeating three-body orbit is chosen. The chosen orbit is a southern L1 Halo orbit in the Earth-Moon system with an orbital period of around 6.57 days. This orbit closely resembles the Near Rectilinear Halo Orbit (NRHO) planned to be used for the lunar Gateway space station. Figure 3 shows this orbit.

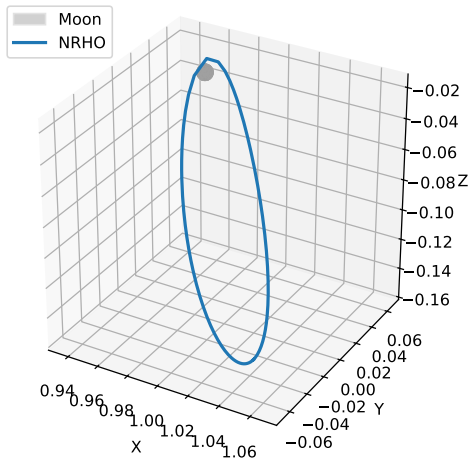


Figure 3: Southern L1 Halo orbit around the Moon resembling the NRHO planned to be used for the future lunar Gateway station.

4.2. Earth-centred observers

The first test case investigates the viability of Earth-centred sensors, particularly a GEO satellite and a ground station on the Earth surface, with the goal of exploring the viability of sensors similar to current SST sensors for cislunar observations. The ground station is positioned in New Norcia on the surface of the Earth while the GEO satellite orbits Earth with an argument of perigee, right ascension and a true anomaly of 0° at the reference epoch of the first of January 2000 at midnight (2000-01-01T00:00:00).

The clear advantage of using Earth-centred observers lies in the accessibility and ease of deployment, especially for Earth ground-based sensors. On the other hand, these observer placements also come with significant drawbacks. The biggest problem for any Earth-centred system in observing the cislunar region results from the large distances between observer and target, severely reducing the apparent brightness of the target. Further limitations also arise from the atmosphere in case of Earth-based ground stations which again limits and distorts the light that is possible to be received from the target. The influence of the atmosphere is not further considered in the presented model. [8]

To get an overview of the observability of the cislunar region, the two Earth-centred sensors are analysed using the lunar target grid. By calculating the average of the apparent magnitude of each grid point over the simulated timespan, the general observability of the grid is investigated.

Figure 4 shows a histogram of the average apparent magnitude cumulated for all grid points. The observed apparent magnitude is displayed on the X-axis and the number of grid points on the Y-axis. From the figure it is clearly visible that the average apparent magnitude, with

a median around 20.5, falls below the observability limit of magnitude 18 for all grid points.

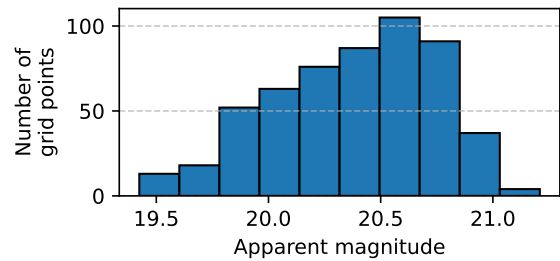


Figure 4: Histogram of the average apparent magnitude of all grid points as observed by the Earth-centred observers.

When taking the observability limit of the sensors into account, the actual observable time of each grid point over the simulated timespan is investigated. Figure 5 shows a histogram of the observable time of each grid point as a fraction of the total simulation time, with the X-axis showing the observable time percentage and the Y-axis representing the number of grid points for which this percentage is applicable. From the figure it is apparent that only around 30 % of all grid points are observable at all and the observable grid points are also only observable for an average of around 10 % of the time.

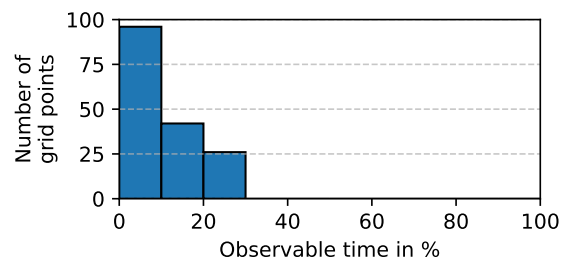


Figure 5: Histogram of the time of observability of all grid points as observed by the Earth-centred observers. The percentage indicates the time fraction of the simulated timespan of one year.

4.3. Moon-based observers

After looking at Earth-centred sensors, the next step is to investigate observers positioned on the Moon. Due to their placement on the Moon's surface, these sensors have significantly smaller distances at which they observe cislunar objects. This in turn has the advantage of a higher apparent magnitude of the targets to the observer, leading to better observability. The placement of observing stations on the lunar surface also comes with drawbacks with the most notable being the logistics of setting up and operating such a ground station. [8]

To investigate the use of lunar ground observers, a single sensor at the south-pole of the Moon will be examined for its ability to observe the cislunar region using the target grid. Due to the negligible change of position of lunar ground stations in the synodic reference frame, observations can only be made in a specific direction, limited by the horizon at the station. To investigate a solution to this problem, a network of six lunar ground stations is also evaluated. The six different ground stations are equally spaced around the Moon in 90° intervals as seen in Figure 6.

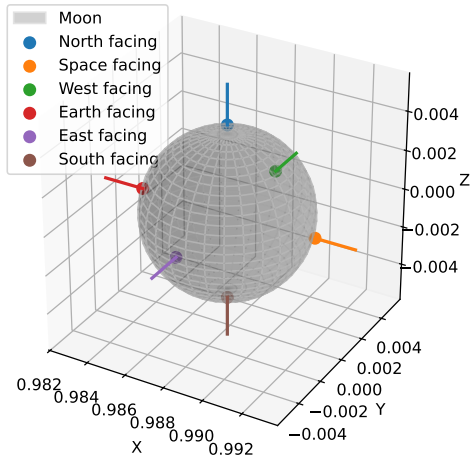


Figure 6: Positions of the Moon-based ground stations on the Moon's surface.

These exemplary positions showcase the possibilities of multiple stations compensating for the visibility restrictions caused by the horizon of the individual stations. The lunar ground sensor network is also evaluated for its general capabilities using the target grid before looking at a specific object in NRHO.

4.3.1. Capabilities of a single Moon ground station

To evaluate the capabilities of a single lunar ground station, an analysis using the ground station at the south-pole is done over the entire lunar target grid. As expected, around 60% of the grid stays unobservable as the observer is limited in its viewing angle by the effective horizon of its position. Looking at the average apparent magnitude over all grid points visible from the Moon station in Figure 7, it is clear that an overall mean apparent magnitude of about 17 already greatly improves observability compared to the Earth-centred observers discussed in Section 4.2.

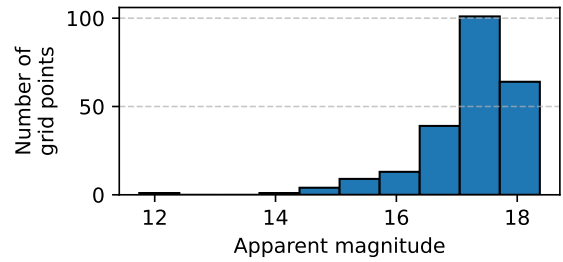


Figure 7: Histogram of the average apparent magnitude of all grid points as observed by a single Moon-based ground observer on the lunar south-pole.

To get a better look at the observability of the region above the horizon for the observer, the observable time fraction can again be plotted in a histogram over all 232 observable grid points, as seen in Figure 8. The figure shows that the target points above the station's horizon, while varying in their observable time fraction, are always observable for more than 50% of the time. While the limiting factor for observability for the Earth-centred observers is in the distance to the target, the limiting factor for the lunar ground-based observers mainly lies in the illumination of the targets by the Sun defined through their phase angle.

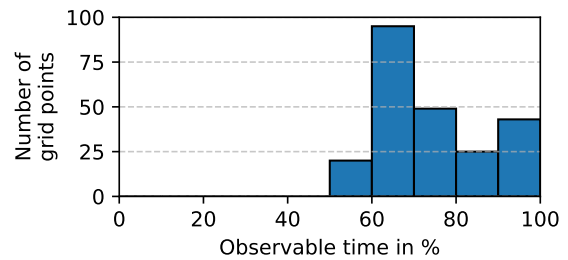


Figure 8: Histogram of the time of observability of all 232 grid points above the horizon as observed by the ground observer on the Moon's south-pole. The percentage indicates the time fraction of the simulated timespan of one year.

4.3.2. Moon ground station networks

After looking at the capabilities of a single lunar ground-based sensor, a number of these sensors in different positions on the Moon's surface are combined to form the afore mentioned lunar ground-based sensor network.

To evaluate the capabilities of this network, the observable time fraction of all grid points over the simulation time can again be drawn into a histogram as seen in Figure 9. This figure shows clearly that, while there are still grid points with poor visibility, the general visibility of the cislunar region is greatly improved by the use of lunar observers compared to Earth-centred observers as described in Section 4.2.

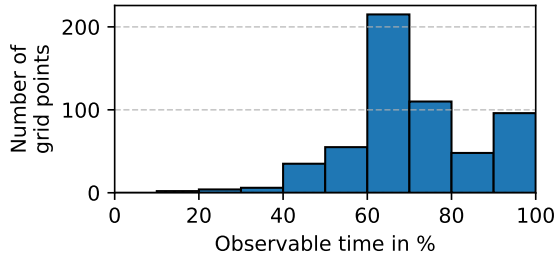


Figure 9: Histogram of the time of observability of all grid points as observed by the network of lunar ground observers. The percentage indicates the time fraction of the simulated timespan of one year.

To get a closer look at the contribution of the individual observers in this network, Figure 10 shows the number of grid points that the different sensors are able to observe at a given epoch over the entire simulation timespan. The fraction of observable grid points over the simulation timespan of one year is displayed for each of the six sensors, following the colour grade on the right. For east, west, space and Earth-facing stations there are periodic time intervals where no observations are possible. This is caused by the Sun which periodically causes white outs for the sensors along the Moon's equator, while the north- and south-facing sensors at the lunar poles do not suffer from the same effect.

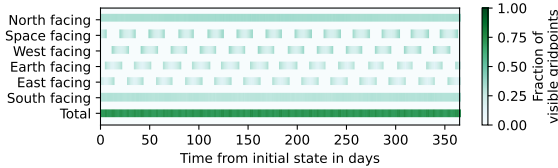


Figure 10: Fraction of all grid points that can be observed by each of the ground observers on the Moon's surface over the span of one year.

As the observable areas of the different sensors overlap, another indication of quality for a sensor network can be investigated by evaluating the redundancy, i.e. the observability of an object by multiple observers simultaneously. For this, the average number of observers for each grid point over the whole simulation timespan is drawn into a histogram as seen in Figure 11. The figure's X-axis represents the average number of observers that can observe a grid point while the Y-axis again represents the number of grid points. The figure shows that for most of the grid points the number of possible observers lies around the total mean of 1.21, with only a few outliers with up to two concurrent or significantly less possible observers. This means that, while in general such a Moon ground-based network provides a good observability of the analysed area, for most grid points no redundancy is achieved with this network architecture.

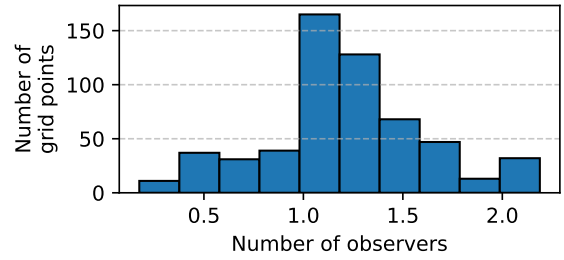


Figure 11: Histogram of the average number of observers for each grid point in the lunar ground station sensor network over the simulation timespan of one year.

4.3.3. Observing NRHO using the Moon ground station network

After the general observability of the region was analysed, a specific example using the NRHO object defined in Section 4.1 is investigated. For observing this object, the lunar ground station network consisting of six separate stations on the Moon's surface is used.

To evaluate the observability of this object over its orbital period, the observable time of the object by each observer in the network is plotted in Figure 12 over the duration of one orbital period of the target. The X-axis represents the time along the orbit starting from the initial starting point which is located at the orbit's apoapsis. The Y-axis again lists the different sensors in the network. The colour grade of the horizontal bars, defined to the right side of the plot, represents the time fraction over the span of one year for which the object is observable by the sensor at the specific orbital position indicated on the X-axis.

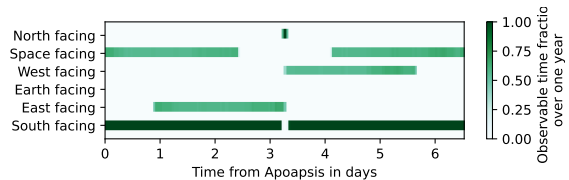


Figure 12: Observability of an NRHO object over its period by each of the ground observers. The colour grade represents the observable time fraction for which the object is observable by the specific sensor.

From the figure it is apparent that the south-facing station is best suited for observing the object for most of its orbital period. This is explained by its position at the pole of the Moon above which the object is residing for most of its orbital period. The north-facing station on the other hand only has a view of the object for a short time around its periapsis when the object passes closely over the lunar north-pole. The observation capabilities of the other ground stations can be explained in a similar fashion.

To get an indication for the redundancy of the sensor network the number of sensors able to observe the object over its orbital period are evaluated. Figure 13 shows the mean number of available observers over the period of the NRHO in days. The X-axis shows the time along the orbital period, starting at the apoapsis of the orbit and the Y-axis displays the mean number of available observers at the specific point of the orbit. Over the span of one year, a mean number of around 1.6 to 2.2 observers can therefore be expected to be able to observe the orbit at any given point in time depending on the object's position on the orbit.

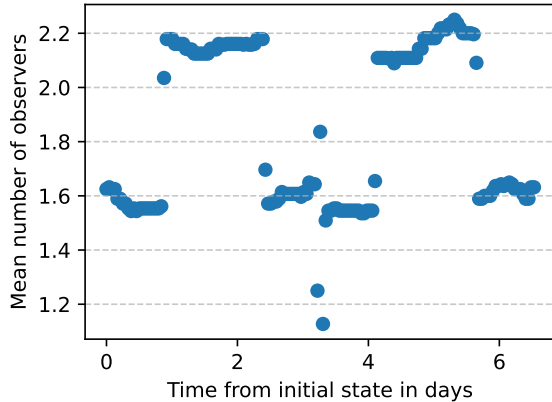


Figure 13: Mean number of possible observers over the orbital period of an NRHO object using the Moon ground-based sensor network averaged over one year.

4.4. Cislunar orbital observers

Similar to the lunar ground-based observers, cislunar orbital observers benefit from the small distances they have to the region and objects they are supposed to observe. One advantage of orbital sensors compared to their ground-based counterparts is the lack of a horizon limiting the possible field of view of the sensor to a specific direction. Due to the orbital sensor's movement through the cislunar region, a large portion of the region can be observed over the span of an orbital period.

On the other hand, the orbital motion of the sensors also brings further complications to the operation of the sensors and observations made using them. The most obvious disadvantage of cislunar orbital sensors is the fact that in reality the repeating orbits used in this model do not exist and are always linked to station keeping efforts in the real world. Further, the position and attitude of these sensors is always associated with a higher uncertainty than their ground-based counterparts, therefore leading to higher measurement uncertainties in the observations as well.

Keeping these advantages and disadvantages in mind, this section takes a look at three cislunar orbital sensor networks. The three sensor networks consist of three, five and seven orbiting sensors on different DRO, Lyapunov

and Halo orbits and were optimised for different metrics, like their observation capabilities and operational cost, by Badura et al [1]. The three sensor networks and their orbits are listed in Table 1 and displayed in Figure 14a, 14b and 14c respectively.

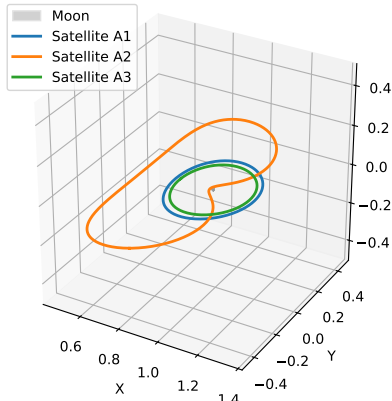
The sensor networks are again analysed to evaluate their general capabilities using the lunar target grid and an exemplary object in NRHO.

4.4.1. Capabilities of the different orbital sensor networks

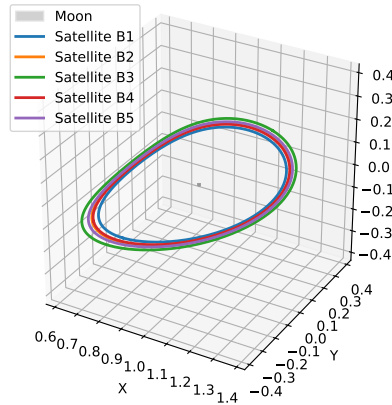
To get an overview of the general performance of the orbiting sensor networks, each network is analysed using the lunar target grid over the whole simulation timespan of one year. For this, the number of grid points that are observable by each of the networks are visualised in Figure 15. In this figure the fraction of all grid points that are observable by the sensors are shown using a colour grade plotted over the simulation timespan on the X-axis. The Y-axis lists all the sensors of the specified network as well as the combined result for the complete network.

The three satellite lunar sensor network and the seven satellite lunar sensor network show a very consistent observability of almost all grid points over the whole timespan, even with frequently changing observability through specific sensors. While the five satellite lunar sensor network in Figure 15b also shows almost full observability of the grid over the full time period, distinct epoch spans become apparent in which the grid observability dips to around 20% for multiple days. Examples for this can be seen at around 90, 180 and 270 days along the simulated timespan axis. This behaviour is due to the chosen orbits and the specific phasing of the satellites in this network, as all five of the observers in the five satellite lunar sensor network are on DROs with a period of around 22 days. These periods of low observability could therefore be improved by routinely adjusting the phasing of the different orbits during actual operations.

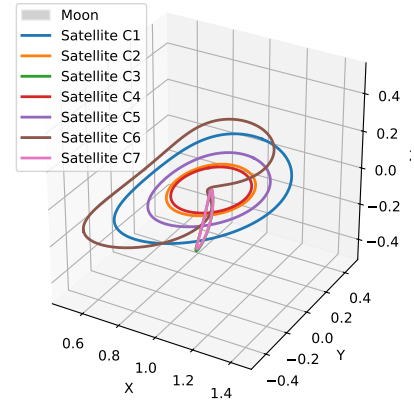
In a similar sense to the number of observable grid points over time, the time fraction, for which the individual grid points can be observed by the network, is investigated next. To visualise this, three histograms for the three sensor networks are displayed in Figure 16 with the observable time fraction shown on the X-axis and the cumulative number of grid points indicated on the Y-axis. While all of the three satellite networks show an observability of over 80% for most of the grid points, the five satellite lunar sensor network only reaches a mean observable time fraction of around 88% while the other two networks show mean observable time fractions of over 90%, as can also be seen in Table 2. This is again explained by the non optimal phasing of the observers in the five satellite lunar sensor network.



(a) Three sensor network as described in [1]. Sensor A2 resides on an L1 Lyapunov orbit while the other two are on DROs.

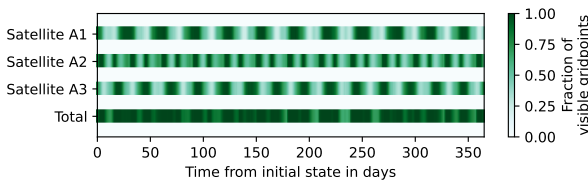


(b) Five sensor network consisting of five DROs, as described in [1].

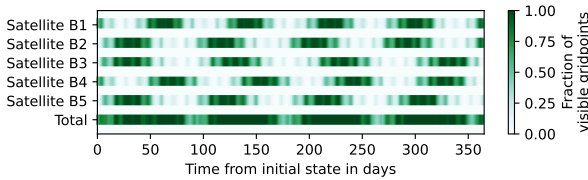


(c) Seven sensor network as described in [1] consisting of four DROs, two southern L1 Halo orbits and on sensor on an L1 Lyapunov orbit.

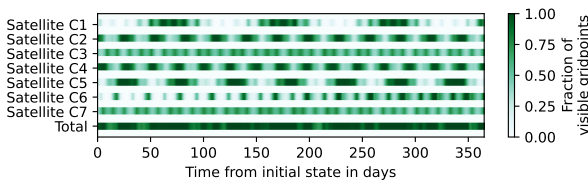
Figure 14: Three cislunar sensor networks using three, five and seven different repeating three-body orbits respectively as described in [1].



(a) Observable grid points for the three satellite lunar sensor network.



(b) Observable grid points for the five satellite lunar sensor network.



(c) Observable grid points for the seven satellite lunar sensor network.

Figure 15: Fraction of all 573 grid points observable by the different observers in the three different lunar orbiting sensor networks over a simulation time span of one year.

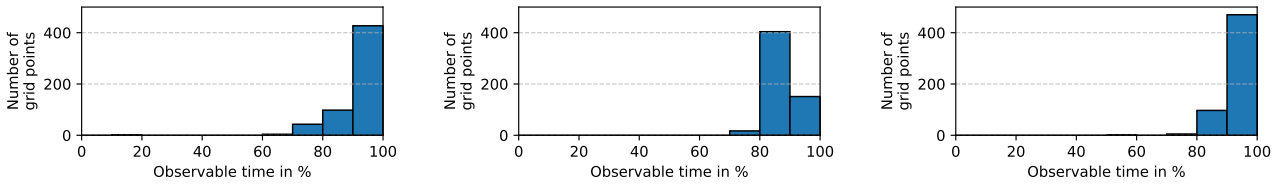
Finally, the redundancy of the three sensor networks in terms of their observation capabilities is analysed. For this, the average number of observers for each grid

point over the whole simulation timespan is investigated. As expected the mean number of available observers increases with the total number of observers in the network, as can be seen in Table 2.

However, when comparing the three sensor networks, the total number of observers does not lead to an equivalent increase in the mean number of available observers nor in the average number of available observers for individual grid points. By dividing the average number of available observers for each grid point by the total number of sensors in the network a quality metric is created showing the observation capabilities per sensor for the given network. This can be interpreted as the capability of the network to observe a certain area per sensor, i.e. a greater value in this metric implies that one sensor can observe a larger area at once, providing observational redundancy with a smaller number of sensors in the network, subsequently making the network more efficient. This quality metric is visualised for all three networks in Figure 17. The histograms for each network show the average number of available observers per grid point divided by the sensor network size on the X-axis, and the cumulative number of grid points on the Y-axis. This shows that the three satellite lunar sensor network provides the best result of observational capability per sensor with a average number of 0.657 available observers per grid point per sensor, i.e. the normalised average number of observers. The seven satellite lunar sensor network achieves a smaller mean number of 0.553 observers per grid point per sensor despite the better performance in terms of observable time fraction, largely due to the fact that the network consists of significantly more sensors. The five satellite lunar sensor network performs the worst out of the three networks in this metric with a mean number of 0.469 observers per grid point per sensor. This is to be

Table 1: The three used orbital sensor networks as described by Badura et al. in [1].

Network	Sensor name	Sensor orbit	Orbital period (days)	Phasing (degrees)
Three satellite network	Satellite A1	DRO	15.253	242.824
	Satellite A2	L1 Lyapunov	29.549	131.412
	Satellite A3	DRO	13.490	1.412
Five satellite network	Satellite B1	DRO	21.423	135.529
	Satellite B2	DRO	22.011	104.471
	Satellite B3	DRO	22.794	232.941
	Satellite B4	DRO	21.913	331.765
	Satellite B5	DRO	22.305	271.059
Seven satellite network	Satellite C1	DRO	22.990	227.294
	Satellite C2	DRO	14.567	208.941
	Satellite C3	L1 Halo Southern	10.771	295.059
	Satellite C4	DRO	13.294	24.000
	Satellite C5	DRO	18.779	230.113
	Satellite C6	L1 Lyapunov	30.195	152.471
	Satellite C7	L1 Halo Southern	10.565	304.941



(a) Histogram for the three satellite lunar sensor network. (b) Histogram for the five satellite lunar sensor network. (c) Histogram for the seven satellite lunar sensor network.

Figure 16: Observable time fraction for each grid point over one year for the three different orbiting lunar sensor networks.

expected as it suffers from the discussed timespans of poor observability seen in Figure 15b) in this metric as well.

While this performance metric for the different networks shows the three satellite network as the most efficient in the observation capabilities per sensor, other factors have to be considered depending on the use case, for example if high redundancy for the tracking of an object is needed or a survey over a region is to be done. In this case the seven satellite network is better suited due to the high average number of available observers, even though the network is less efficient on a per sensor basis.

4.4.2. Observing NRHO with lunar orbital sensor networks

After investigating the general observation capabilities of the three selected sensor networks in the cislunar region, a specific example is examined observing an orbiting object in NRHO around the Moon. For this, the three satellite lunar sensor network is used due to

its capabilities compared to the other two networks discussed in Section 4.4.1.

To evaluate the capabilities of the sensor network in observing the NRHO target object, the observable time fraction is investigated. The observable time fraction is visualised in Figure 18 where the X-axis represents the time over one orbital period of the target starting at its apoapsis, and the colour gradient of the horizontal bars represents the time fraction it is observable for at this point of its orbit during the simulation time span of one year. The Y-axis lists the three sensors of the used sensor network.

Table 2: Mean values for observable time fraction and number of available observers for all grid points for the three different orbital sensor networks (averaged over all grid points).

Sensor network	Three satellite network	Five satellite network	Seven satellite network
Mean observable time fraction	92.95 %	87.58 %	94.53 %
Mean number of available observers	1.97	2.34	3.87
Mean normalised number of observers	0.657	0.469	0.553

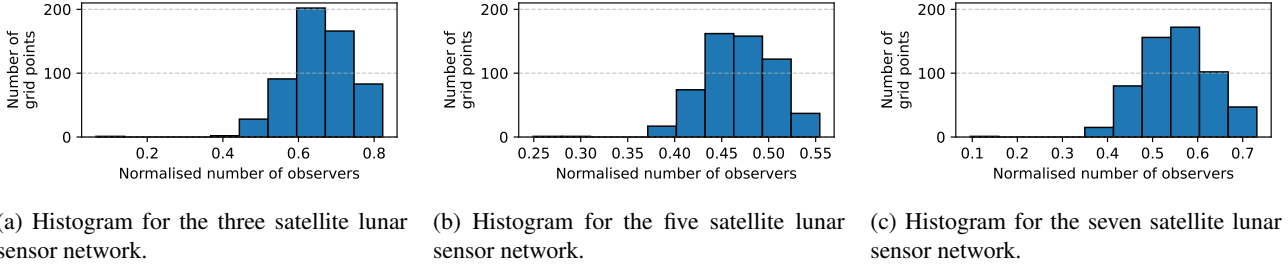


Figure 17: Histogram of the average number of available observers for each grid point per sensor for each of the three different orbiting lunar sensor networks over the span of one year.

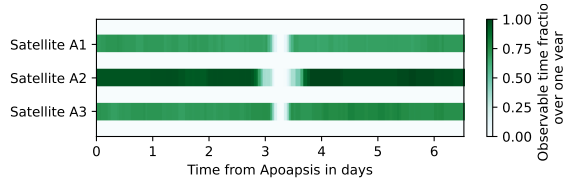


Figure 18: Fraction of observable time over the orbital period of an NRHO by each of the orbiting sensors in the three satellite lunar sensor network over the span of one year.

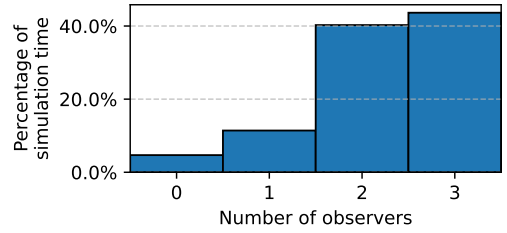


Figure 19: Histogram of the number of available observers for the NRHO target object for the three satellite lunar sensor network over the simulation time span of one year.

In Figure 18, a lack of observability in the middle of the objects orbital path at around 3.3 days becomes apparent. This is to be expected with any of the sensor networks as the target at this point is at its periapsis and therefore close to the Moon, making it hard to detect due to white out. While the target is nearly impossible to observe at periapsis, the general observability for the rest of the target’s orbit is above 50 % for all sensors in the network.

After looking at the general observable time fraction of the target by the sensor network, the redundancy in the observation capabilities is evaluated. Figure 19 shows how many sensors can observe the target concurrently over the full simulation timespan of one year. The X-axis displays the number of observers while the Y-axis shows the percentage of the simulation timespan. With an average number of 2.23 available observers and more than two available observers for over 80 % of the time, the network displays a solid redundancy for the task of observing the target.

5. CONCLUSION AND OUTLOOK

In this paper a model was presented for analysing the observability of the cislunar region using different sensors and sensor networks, ranging from Earth-based observatories to orbiting sensor networks on repeating cislunar orbits. The model is built on the assumptions of the CR3BP and utilizes GODOT’s functionalities for various astrodynamical tasks. The model is developed as a basis for running analyses of various configurations of different sensor and target variations to evaluate the observational capabilities of said sensors. To showcase this, some first results of exemplary analyses using different sensors and sensor networks were presented:

Firstly, the viability of Earth-based and Earth-centred sensors for observations in the cislunar region were evaluated using an exemplary Earth ground-based observatory and a GEO satellite. A similar conclusion

could be reached as presented by Holzinger et al in [8] with the large distances of the sensors to the cislunar targets creating a challenging environment for detecting the targets due to their low brightness.

Next, the use of lunar ground-based sensors was investigated in terms of their single observer capabilities as well as clustered into a network spread over the lunar surface. As expected, their significantly closer distance to the observed region resulted in better observation capabilities. While single sensors are not capable of observing the whole regions due to the Moon's horizon, well placed ground observers can still provide good observations for specific orbits. By spreading multiple sensors over the surface the limitation due to their horizon can also be overcome.

Finally, three sensor networks utilising orbiting sensors on repeating cislunar trajectories, optimized for cislunar observations by Badura et al [1], were investigated. The three sensor networks were analysed regarding their capabilities to observe the selected cislunar region. As expected, all three of the networks are very capable of observing the region confirming the results of [1]. Further, the observation capabilities of one network in observing a specific object on an NRHO was evaluated. While the general performance of the sensor network was very good, an observation of the object close to the Moon at periapsis was not possible.

After successfully showing the possibilities of evaluating the observation capabilities of selected sensor networks, future work will expand on this model by not only evaluating observability but also trackability of cislunar objects specifically in the context of Space Situational Awareness and Space Surveillance and Tracking. Using uncertainty propagation to estimate the measurement uncertainty of observed objects, trajectories can be predicted, leading to more quality metrics for different sensor networks.

The limited area around the Moon, used for analyses in this work, can be expanded outwards and towards the L1 and L2 libration points for a better overview of the whole cislunar region. Further, the surroundings of the L4 and L5 libration points can also be analysed in a similar manner. With the expansion of the considered area, different objects in different orbits can be considered as well. This expansion also calls for further investigation and evaluation of sensor networks which are specialised for different areas in the cislunar region.

REFERENCES

1. Badura G., (2023). Optimizing Distributed Space-Based Networks for Cislunar Space Domain Awareness In the Context of Operational Cost Metrics, *Proceedings of the Advanced Maui Optical and Space Surveillance (AMOS) Technologies Conference*
2. Bhadauria S., Frueh C., (2022). Optical observation regions in cislunar space using the bi-circular restricted

- four body problem geometry, *Proceedings of the 2022 Advanced Maui Optical and Space Surveillance Technologies Conference*
3. Eapen R.T., Paul S.N., Singla P., (2024). Sensor Tasking Strategies for Space-Based Observers in the Cislunar Environment, *AIAA SCITECH 2024 Forum*
4. ESA, GODOT library documentation, url: "<https://godot.io.esa.int/godotpy/>", accessed 13.03.2025
5. Folta D.C., et al., (2015). An Earth–Moon system trajectory design reference catalog, *Acta Astronautica*, **110**, 341-353
6. Frueh C., et al, (2021). Cislunar space situational awareness, *31st AAS/AIAA Space Flight Mechanics Meeting*
7. Hejduk M.D., (2011). Specular and diffuse components in spherical satellite photometric modeling, *Proceedings of the Advanced Maui Optical and Space Surveillance Technologies Conference*
8. Holzinger M.J., Chow C.C., Garretson P., (2021). A Primer on Cislunar Space, Air Force Research Laboratory
9. Johnson N. L., (1993). US space surveillance, *Advances in Space Research*, **13**(8), 5-20
10. JPL, Three-Body Periodic Orbits, url: "https://ssd.jpl.nasa.gov/tools/periodic_orbits.html", accessed 29.01.2025
11. NASA, Artemis, url: "<https://www.nasa.gov/feature/artemis/>", accessed 13.03.2025
12. NASA, Commercial Lunar Payload Services, url: "<https://www.nasa.gov/commercial-lunar-payload-services/>", accessed 13.03.2025
13. NASA, Intuitive Machines 3, url: "<https://nssdc.gsfc.nasa.gov/nmc/spacecraft/display.action?id=IM-3-NOVA>", accessed 13.03.2025
14. Peldszus R., Faucher P., (2022). European union space surveillance & tracking (EU SST): State of play and perspectives, *Space Policy*, **62**
15. Svensson U., Savioja L., (2024). The Lambert diffuse reflection model revisited, *The Journal of the Acoustical Society of America*, **156**(6), 3788-3796
16. Vallado D., (1997). *Fundamentals of Astrodynamics and Applications*, Springer and Microcosm Press
17. Zhaoyu P., Qiong W., Yaosi T., (2015). Technology roadmap for Chang'E program, *Journal of Deep Space Exploration*, **2**(2), 99-110